Falsifying computational models of angiogenesis through quantitative comparison with in vitro models

Vergroesen, T.M.; Vermeulen, V.; Merks, R.M.H.

Falsifying computational models of angiogenesis through quantitative comparison with *in vitro* models

Tessa M. Vergroesen[1], Vincent Vermeulen[1], Roeland M. H. Merks[1,2]

[1]Institute of Biology, Leiden University, Leiden, The Netherlands

[2]Mathematical Institute, Leiden University, Leiden, The Netherlands

Abstract

During angiogenesis, endothelial cells migrate from existing vessels, proliferate and collectively organize into new capillaries. *In vitro* and *in vivo* experimentation is instrumental for identifying the molecular players and cell behavior that regulate angiogenesis. Alongside experimental work, computational and mathematical models of angiogenesis have helped to show if the current molecular and cellular understanding of cell behavior is sufficient. As input, the model takes (a subset of) the current knowledge or hypotheses of single cell behavior and captures it into a dynamical, mathematical description. As output, it predicts the multicellular behavior following from the actions of many individual cells, e.g., the formation of a sprout or the formation of a vascular network. Paradoxically, computational modeling based on different assumptions, i.e., completely different, sometimes non-intersecting sets of observed single cell behavior, can reproduce the same angiogenesis-like multicellular behavior, making it practically impossible to decide which, if any, of these models is correct. Here we present dynamic analyses of time-lapses of *in vitro* angiogenesis experiments and compare these with dynamic analyses of mathematical models of angiogenesis. We extract a variety of dynamical characteristics of endothelial cell network formation using a custom time-lapse video analysis pipeline in ImageJ. We compare the dynamical network characteristics of the *in vitro* experiments to those of the cellular networks produced by computational models. We test the response of the *in silico* dynamic cell network characteristics to key model parameters and make related changes in the composition of the *in vitro* environment. We present comparisons with computational model outcomes and argue how models that fail to reproduce these trends can be rejected. All in all, we show how our dynamic approach helps to clarify key endothelial cell

interactions required for angiogenesis, and how the approach helps analyze what key changes in network properties can be traced back to changes in individual cell behavior.

Keywords: angiogenesis, image analysis, model falsification, endothelial cells, cellular Potts model

Introduction

Angiogenesis, the formation of new blood vessels from existing ones, is crucial for physiological and pathological mechanisms such as embryonic development, wound healing and tumor growth. Pro-angiogenic factors, including vascular endothelial growth factor A (VEGF-A), stimulate sprouting in endothelial cells (ECs), which make up the inner lining of blood vessels (1–3). The ECs proliferate and migrate into the extracellular environment and form a vascular network that supplies the surrounding tissue with nutrients and oxygen and removes waste products. A key regulatory factor determining the final structure of the new blood vessel network is the composition of the extracellular matrix (ECM), the scaffold of proteins that surrounds the blood vessels and provides structural support to the newly formed multicellular network (4). Specific integrin binding sites on ECM proteins like collagens, fibronectin and laminins allow cells to exert stresses on the ECM and sense the mechanical properties of their environment (5). Cells also secrete enzymes which digest the ECM, releasing ECM-retained growth factors, including VEGF-A, which stimulate EC migration (6). Cell-cell interactions, like Notch signaling and vascular endothelium cadherin (VE-cadherin) adhesions, regulate individual cell behavior within the network, separating the cells into leading tip- and proliferating stalk cells (2). In response to VEGF-A, cells upregulate Delta-like 4 (DLL4). DLL4 activates NOTCH1 in neighboring cells, which subsequently downregulates VEGF receptor (VEGFR)-2 expression (7). Similarly, VE-cadherin inhibits VEGFR-2 signaling, making the cells less susceptible to VEGF, resulting in less angiogenic potential of the cells (8). The combination of extracellular, intercellular and intracellular regulation makes angiogenic sprouting a complex and multiscale process. An understanding of how each regulatory mechanism contributes to the final network formation is necessary for biomedical applications where angiogenesis needs to be stimulated, steered or reduced, like tissue engineering (9) or vascular normalization (10).

One of the more commonly used *in vitro* models to test the effect of environmental changes on angiogenesis is the tube formation assay (TFA) (11). In this assay ECs are placed on top of a basement membrane-like substrate, where the ECs, under the right conditions, spontaneously organize into networks of interconnected tubes. With this assay the influence of various chemical and mechanical stimuli on EC networks has been investigated by comparing the final network between conditions (12). In the analysis of TFA outcomes it is often assumed that a network that contains a higher density of branches indicates a higher angiogenic potential of the cells (i.e., more sprouting). However, the temporal development of the network over time may contain key information on the dynamic processes regulating angiogenesis. Merks *et al*. (2006), therefore, measured the density of branch points in developing vascular networks *in vitro* at regular intervals and observed that the network density dropped slowly over time (13). Parsa *et al.* (2011), analyzed time-lapse videos of *in vitro* angiogenesis in more detail, and described the development of endothelial networks as a carefully orchestrated sequence of five subevents: [1] rearrangement and aggregation, [2] spreading, [3] elongation and formation of cell–cell contacts, [4] plexus stabilization, and [5] plexus reorganization (14). The first two stages describe the attachment of the cells to the substrate directly after cell seeding. The rate and the extent of cell spreading on the substrate have been linked to substrate stiffness and composition (15) and are assumed to be influenced by the traction forces cells are able to exert on the substrate (16). Later stages in the tube formation assay rely on a combination of cell-cell and cell-ECM interactions. Rüdiger *et al.* (2020) observed a collapse of EC networks on soft, laminin matrices, confirming the importance of the ECM to provide support for the network to stabilize (4).

Computational modeling is a helpful tool for proposing and testing whether hypothetical developmental mechanisms are sufficient to explain biological observations (17). Different computational models of *in vitro* angiogenesis all consider angiogenesis as the assembly of ECs into a vascular-like network structure (18–20). For example, in Manoussaki *et al.* (1996), the *in vitro* matrix remodeling behavior of ECs on gelled matrix is described with a continuum model, in which ECs are described as local densities using a system of differential equations (21). Similarly, in Serini *et al.* (2003), ECs are modeled to migrate upwards a chemoattractant gradient with a continuum model (22).

In Palachanis *et al.* (2015), ECs are considered as identical 2D ellipses, using a single-particle model (23). Köhn-Luque *et al.*, (2013) used a hybrid continuum and cell-based model to model the effect of VEGF retention in the ECM on EC network formation (6). In cell-based models of angiogenesis, ECs are described as discrete areas of variable shapes, where multicellular behavior arises from the response of single cells to inputs from their microenvironment (24,25). Similarly, Vega *et al.* (2020) used a hybrid continuum and cell-based model to model the interaction between Notch- and VEGF signaling and cell-ECM adhesion (26).

Interestingly, both continuum models, particle-based models, as well as cell-based models are successful in mimicking EC network formation, and different hypotheses, or model inputs, can in some cases lead to a qualitatively similar output. In this work we focus on three cell-based models as previously developed in our group (13,27,28). The “cell elongation model” assumes that ECs are attracted towards one another through autocrine/paracrine signaling by secreting a chemoattractant (13). In this model it was observed that cells self-organize into vascular-like structures if the cells have an elongated shape. Observations by Parsa *et al.* (2011) support the necessity for ECs to elongate to form networks, as cells elongate before they start forming a network and continue to elongate as the network develops (14). The “contact-inhibition model” also assumes that ECs are attracted to one another through a secreted chemoattractant, but here it was assumed that VE-cadherin binding mediates contact-inhibition of chemotaxis, following observations by Dejana *et al.* (2004) that VE-cadherin-VEGFR2 complex forming limits cell proliferation (29) and that in the yolk sac of VE-cadherin double-knockout mice and in *in vitro* mouse allantois explants ECs failed to form vascular networks and aggregated into isolated islands (28,30). In disagreement with VEGF guided cell-cell attraction-based models, Rüdiger *et al.* (2020) observed persistent network formation in the absence of a VEGF-A gradient and they argue that the *in vitro* network formation is driven by mechanical communication (4).The importance of cell-ECM interactions is further supported by observations by Stephanou *et al.* (2007), where they observed faster and more lacunae in network formation on fibrinogen gels of intermediate rigidity (31). Finally, the “mechanical cell-cell communication model” assumes that ECs are attracted to one another solely through mechanical interaction with the ECM

(27). In this cell-ECM interaction model ECs induce strain in the ECM through contractile forces and migrate up the strain gradient (27). With these many models that successfully reproduce multicellular network formation based on different observed EC behavior, we need to critically exam these models to see which assumptions, if any are correct.

Thus, for a more complete understanding of the integration of different mechanisms driving angiogenesis, we must quantitatively compare these computational models to *in vitro* experiments by systematically changing model parameters and *in vitro* experimental setup and iteratively refining the models based on the outcomes of the comparison. As an initial step, we will critically examine three models originating from our own research group: [1] The cell elongation model (13); [2] the contact inhibition model (28); and [3] the mechanical cell-cell communication model (27). For this comparison, dynamical analyses of *in vitro* experiments are required. Here we present new dynamic time-lapse videos of tube formation assays and a new analysis pipeline based on ImageJ and demonstrate its use for model selection for network formation. There are commercial and open-source image analysis tools available for quantitative analyses of angiogenic networks (32–35), however these tools are designed for single frame end-point analyses and therefore less suitable for high-throughput dynamical analyses of large quantities of data. Our novel image analysis pipeline is suitable to dynamically analyze and compare *in vitro* and simulated networks. The pipeline allows us to reliably extract network features over time, such as the branch density and length and the average size and number of lacunae. In this study we use this pipeline to compare the output of three cellular Potts models of 2D angiogenesis (13,27,28) to *in vitro* experiments over time at different cell densities and find that the distance at which cells are able to communicate with each other determines the features of the final, stabilized network, but the speed and manner at which the networks stabilize depends on other characteristics of the cell communication, like the speed at which the cell attracting signal spreads.

Results

Quantification of *in vitro* endothelial network dynamics

To understand and compare the dynamic behavior during *in vitro* and *in silico* EC network formation, we developed an image analysis pipeline to extract network characteristics from 2D angiogenesis timelapses and applied it to *in vitro* and *in silico* networks. To capture *in vitro* EC network formation ECs were seeded on a Matrigel matrix and imaged in phase contrast for 24 hours with an interval of 15 minutes (Fig 1A). The ECs in the timelapse images were segmented from the background using a combination of Gaussian denoising and local variance extraction, followed by Huang thresholding (S1 Fig). Network features were extracted from the segmented timelapses for each timestep using FIJI plugins Analyze Skeleton and Analyze Particles (Fig 1B). For the *in silico* networks we selected three cell-based computational models of 2D angiogenesis (13,27,28) and extracted the network characteristics directly from the output images using the same image analysis pipeline as the segmented *in vitro* timelapses.

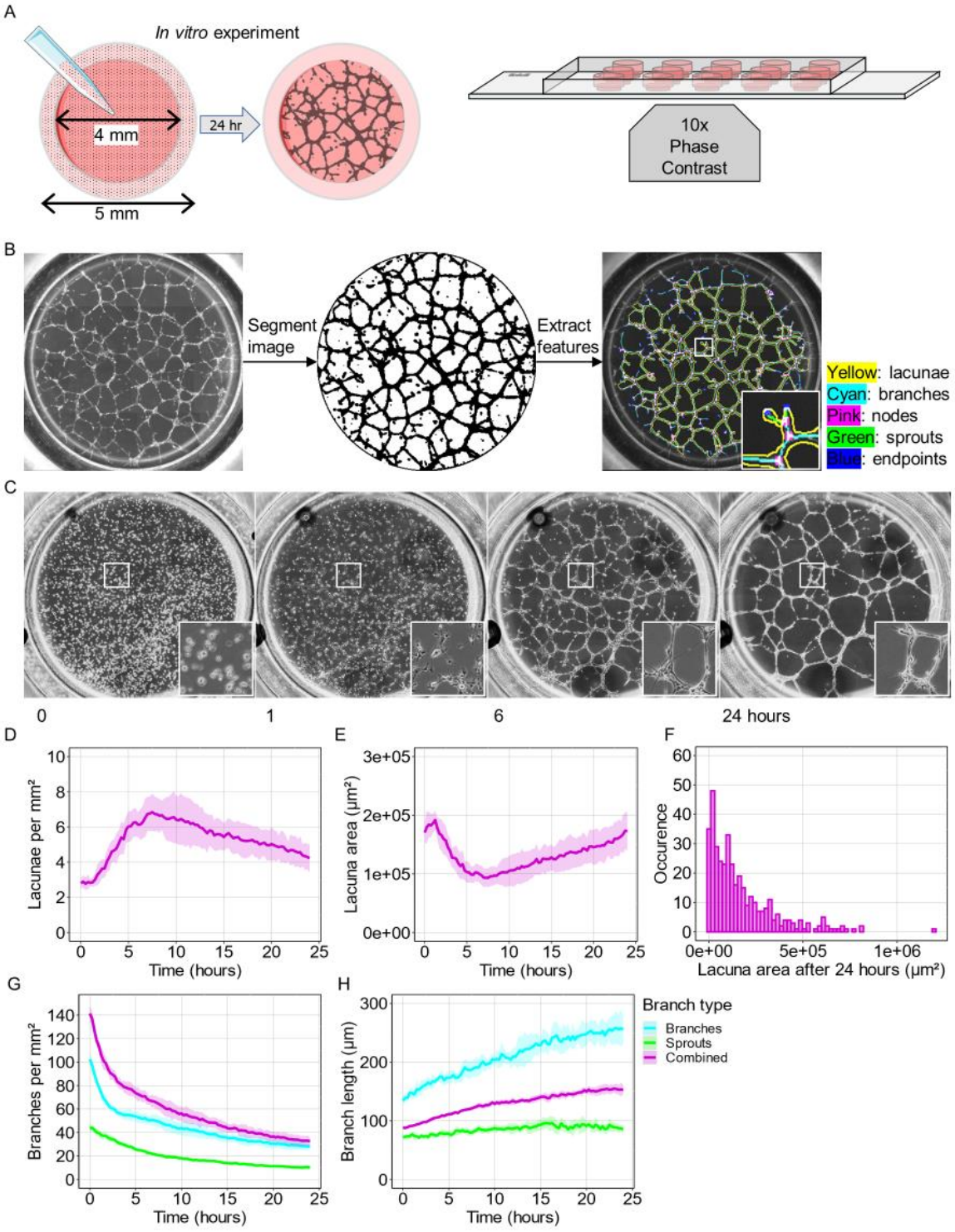

Figure 1. Image analysis pipeline for *in vitro* phase contrast timelapses. A) Graphic summary of *in vitro* experiment. B) Networks were segmented from the background and labeled in FIJI. Insert is 350 x 350 µm². C) ECs were seeded on GFR Matrigel, and network formation is captured in phase contrast for 24 hours with intervals of 15 minutes. Insert is 500 x 500 µm². D-G) Quantitative analysis of (D-F)

lacunae and (G-H) branches under standard conditions. Shaded area represents a standard deviation of eight wells on one slide.

In the *in vitro* culture under standard conditions, the ECs started forming cell-cell connections within the first hour after seeding on a Matrigel matrix and thereafter self-organized into fully connected networks within six hours (Fig 1C). We were able to divide the development of the network characteristics over time in three distinct parts, which we describe following Parsa *et al.* (14), as: [1] The first hour resembled stages 1 and 2, "rearrangement and aggregation", followed by "spreading" (Fig 1C). In these stages the ECs were randomly dispersed on top of the Matrigel and started to form attachments to the ECM. The next 6 hours matched Parsa's stage 3, "elongation and formation of cell-cell contact". During this stage new connections formed between ECs, which is reflected in an increase in the number of lacunae from 2.78 ± 0.34 to 6.84 ± 1.06 per mm² (Fig 1D). Hereafter, the number of lacunae decreased linearly in time (R^2=0.91, p-value < 0.001), resembling Parsa's stage 4 and 5: "plexus stabilization" and "reorganization". The average lacuna area displayed a linear increase due to a higher occurrence of lacuna merging and smaller lacunae closing compared to the formation of new lacunae (Fig 1E) (R^2=0.93, p-value < 0.001). The number of branches within the network continuously decreased and their average length increased (Figs 1G and H). During the first three stages branches predominantly increased in length due to merging of branch sprouts, but during stages 4 and 5 we observed an increase in merging of existing branches.

In silico models can be adjusted to resemble *in vitro* networks

To compare the dynamics of *in silico* networks to the *in vitro* networks we selected model parameters that mimic the *in vitro* experiment. To represent the inner well of the *in vitro* experiments (Fig 1A), ECs were simulated within a circular field with a diameter of 1900 lattice sites for the two chemotaxis models (1 lattice site = 2 x 2 μm) and 760 lattice sites for the mechanical model (1 lattice site = 5 x 5 μm) (Fig 2A). To select the parameters that determine the target area and length of the simulated cells, we measured cell areas and diameters in fluorescently labeled ECs within network timelapses (S2 Fig). We observed an average cell area of 1052 ± 596 μm² after three hours (S2 Fig), with a cell length of 90 ± 21 μm for elongated cells (S2 Fig). Based on these measurements we set the target area for the

simulated cells to 250 lattice sites (chemotaxis models) and 40 lattice sites (mechanical model), which corresponds to a physical area of 1000 μm². In the elongated cell model, we set the target length to 45 lattice sites, which corresponds to 90 μm.

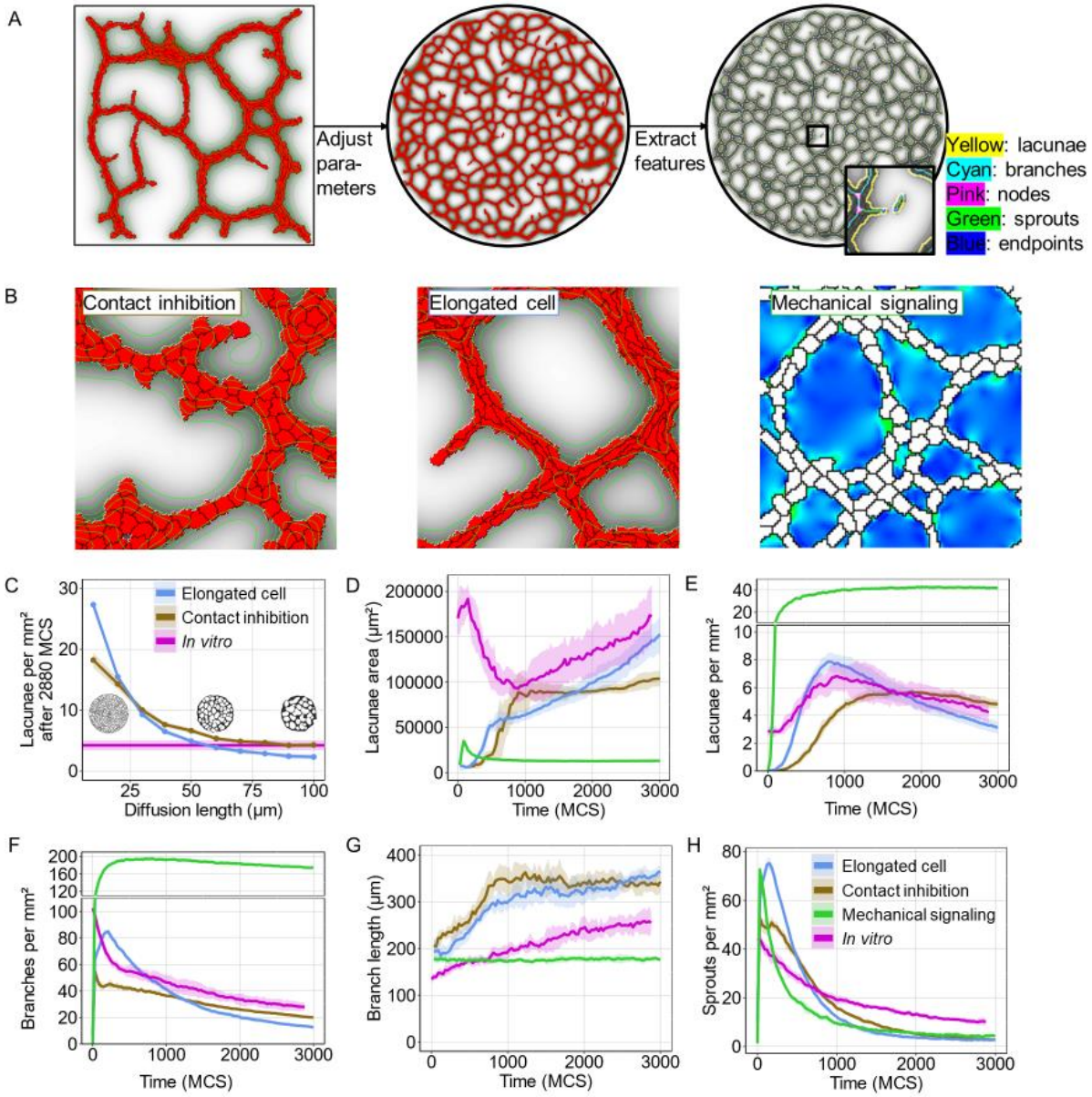

Figure 2. Quantitative comparisons between two chemotaxis-based models and a mechanical model of 2D angiogenesis to *in vitro* timelapse results. A) The model parameters are adjusted to resemble the *in vitro* situation and network characteristics are extracted using the same image analysis pipeline as the *in vitro* networks. B) Simulated ECs were placed on a circular grid and run for 6000 Monte Carlo steps (MCS). In the chemotaxis models ECs (red) excrete a chemoattractant (grey) that diffuses through the medium (white). In the mechanical model ECs (white) exert strain on their

environment (green/blue heatmap) (Field area is 500 x 500 µm². C) A comparison of the number of lacunae per mm² for chemoattractant diffusion lengths ranging from 10 µm to 100 µm for the elongated cell model and the contact inhibition model. In magenta the *in vitro* number of lacunae per mm² after 24 hours. Inserts show the elongated cell model for a diffusion length of 10, 50 and 100 µm. D-G) Quantitative analysis of (D, E) lacunae and (F, G) branches *in vitro* (magenta) and in the elongated cell model (blue), the contact inhibition model (golden) and the mechanical model (green). H) The number of sprouts, branches connected to a single node *in vitro*, in the elongated cell model, the contact inhibition model and the mechanical model. ($D = 5.0 \cdot 10^{-13}\ m^2 s^{-1}, \epsilon = 1.02 \cdot 10^{-4}\ s^{-1}, \alpha = 1 \cdot 10^{-3}\ s^{-1}$). Shaded area represents standard deviation of eight simulations or eight *in vitro* timelapses.

In the elongated cell model, ECs secreted a chemoattractant, migrated upwards the chemoattractant gradient and elongated towards a target length (13). In the contact inhibition model ECs secreted a chemoattractant and migrated upwards the chemoattractant gradient, but locally inhibited chemotaxis in their neighbors (Fig 2A) (28). To find the parameters that describe the chemoattractant in the two chemotaxis models for which the models most resemble the *in vitro* networks (i.e., the diffusion coefficient, the decay rate and the secretion rate) we investigated the effect of the diffusion length of the chemoattractant on the network formation. Diffusion length (l_D) depends on the diffusion coefficient (D) and the decay rate (ϵ) of the chemoattractant according to $l_D = \sqrt{\frac{D}{\epsilon}}$. Therefore we altered the diffusion length from $l_D = 10\ \mu m$ to $l_D = 100\ \mu m$ with steps of 10 µm by varying the decay rate of the chemoattractant, while keeping the diffusion coefficient constant at $D = 5 \cdot 10^{-13}\ m^2 s^{-1}$ (Fig 2C). For a full list of the selected parameters, see S1 Table. *In vitro*, the average number of lacunae per mm² after 24 hours was 4.23 ± 0.81, with an average lacuna area of 0.17 ± 0.03 mm² (Fig 1D and E). When we increased the diffusion length in the two chemotaxis model, we observed that the average number of lacunae decreased (Fig 2C), in agreement with previous work (13,28).

Based on the outcome of the comparison of the number of lacunae, we selected a decay rate of $\epsilon = 1.02 \cdot 10^{-4}\ s^{-1}$, which corresponds to a diffusion length of $l_D = 70\ \mu m$. This resulted in an average number of lacunae after 2880 MCS of 3.27 ± 0.47 per mm², with an average area of 0.15 ± 0.02 mm² for the elongated cell model and 4.88 ± 0.35 per mm², with an average lacuna area of 0.10 ± 0.01 mm² for the contact inhibition model (Figs 2D and E). With the selected diffusion length of $l_D = 70\ \mu m$, we observed some similarities between the dynamics of the model outcomes and the *in vitro* networks: During the initial relaxation time (100 MCS) the ECs in the models reached their target size and shape, which mimics stages 1-3 of the 5 stages described in (14): cell spreading and elongation. Next, we looked at the formation of cell-cell connections as ECs started excreting chemoattractant. The increase in cell-cell connections could be indicated by the decrease in number of branches (Fig 2F). The transition towards stage 4, stabilization of the network, was more gradual in the contact inhibition model than in the *in vitro* networks and in the elongated cell model (Fig 2E). The number of lacunae decreased faster in the elongated cell model than in the contact inhibition model (Fig 2E) and for the first 1680 MCS we observed fewer and larger lacunae in the contact inhibition model than in the elongated cell model. The number of branches was initially larger in the elongated cell model than in the contact inhibition model. In agreement with the *in vitro* networks, the branch number decreased quasi-exponentially in the elongated cell model, whereas in the contact inhibition model the number of branches decreased more linearly (Fig 2F). Both chemotaxis-based models have longer branches than the *in vitro* networks (Fig 2G). This difference in branch number and length could partially be explained by the higher number of sprouts detected *in vitro* than in the models (Fig 2H). Sprouts are branches that are connected to a single node and the Analyze skeleton tool splits an existing branch into two each time a sprout appears, resulting in two shorter branches.

In the mechanical model, the ECs are assumed to stiffen the ECM through the exertion of traction forces on their environment and move upwards the stiffness gradient (Fig 2B) (27). We selected a Young's modulus of 12 kPa, with a Poisson's ratio of 0.45, based on the original work. For a full list of the selected parameters, see S2 Table. For the selected parameters, cells formed a dense network of branches with small lacunae. The composition this network was similar to an early-stage endothelial

network. This suggests that in the present form of the mechanical model, the mechanical model successfully reproduces the network formation phases (phases 1-3), but it did not describe the remodeling phases well.

Another noticeable difference between the three models and the *in vitro* networks was the composition of the branches (Figs 1B and 2B). *In vitro* the cell-covered area decreased over time as cells move on top of each other, whereas in the *in silico* models the cell-covered area remained constant (S2 Fig). This is likely caused by the fact that *in vitro,* the ECs are able to crawl on top of each other, thus forming thin branches and thick nodes, which is impossible in the two-dimensional cellular Potts model.

Increasing cell density results in an initial increase in number of branches and lacunae *in vitro*

To investigate whether the models respond similarly to a change in the initial conditions as *in vitro* networks, we next analyzed network formation at different cell densities. Previous *in vitro* studies on primary endothelial cells observed an inability for the cells to form tubes under or over a threshold density, similar to a percolation threshold (4,22). Consistent with these previous results, we observed that HMEC-1 cells retained the ability to form cell-cell connections and short branches at 1000 ECs per well (80 cells/mm^2), however, they were not able to form a network spanning the full well (Fig 3A). Over 2000 ECs per well (160 cells mm^2), we observed the development of a fully connected network spanning the entire well (Fig 3A). With more cells per well a higher number of lacunae and branches formed within the first hours, but for more than 4000 cells per well (320 cells mm^2), the networks converged onto the same number of lacunae, branch number and branch length (Figs 3B-D).

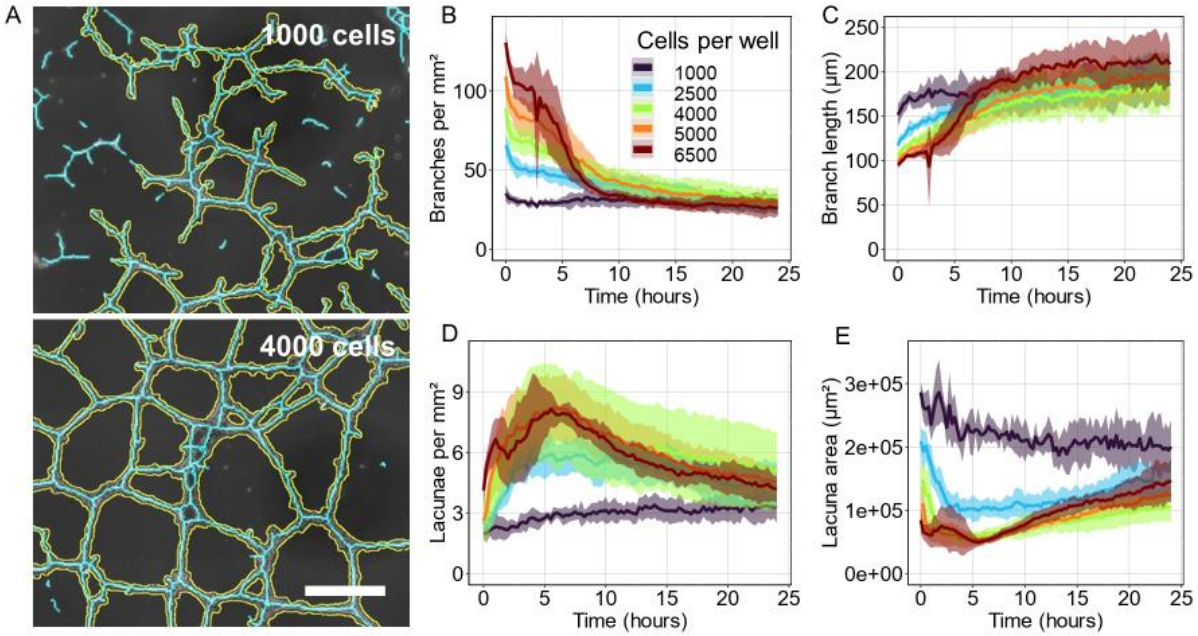

Figure 3. A comparison of the response of *in vitro* networks and model outcomes to higher seeding density. A) Segmented *in vitro* networks with an inner well cell count of 1000 (left) and 4000 (right). B-E) Quantitative analysis of (B, C) branches and (D, E) lacunae for different cell densities. Scale bar = 500 µm. Shaded area represents standard deviation of 5 or 6 wells from two separate experiments.

The cell elongation model response resembles that of the *in vitro* networks to a change in cell density

Whereas a higher cell density caused an initial increase in the number of branches for all three *in silico* models, this difference diminished as the network remodeled in the two chemotaxis-based models (Figs 4A-F), similar to what we observed *in vitro* (Fig 3B). The mechanical model had a much higher number of branches and the difference between branch number for different cell densities persevered for much longer than in the chemotaxis-based models and the *in vitro* timelapses (Figs 3B and 4C). Out of the three models, the elongated cell model most resembled the *in vitro* network response to a change in cell density, even when subjected to a range of diffusion lengths.

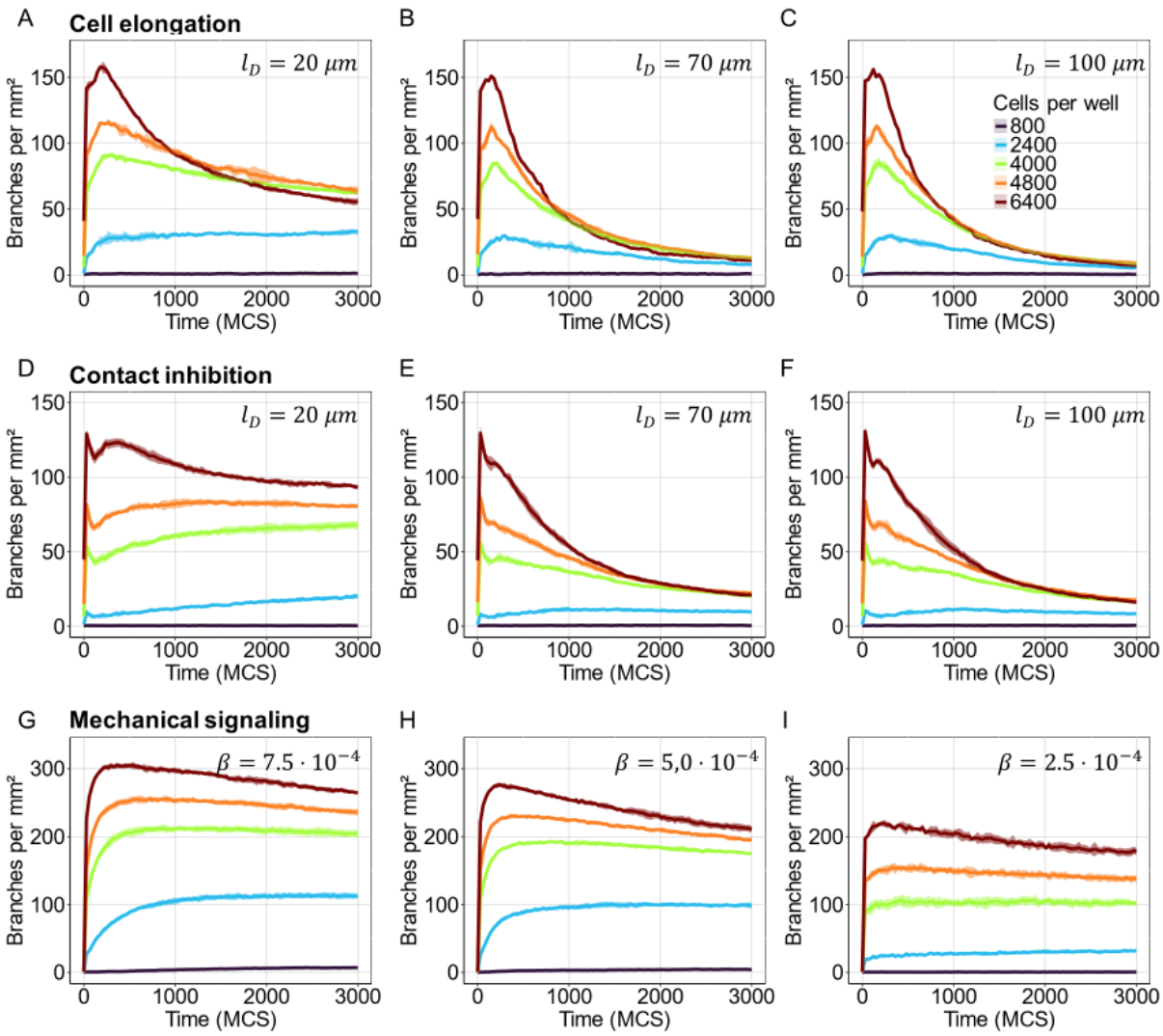

Figure 4. A comparison of the response of model outcomes to higher seeding density. Quantitative analysis of the number of branches for different cell densities with different diffusion lengths (l_D) in the (A-C) elongated cell model and (D-F) the contact inhibition model, and different stiffness sensitivity (β) (G-I) in the mechanical model. ($D = 5.0 \cdot 10^{-13}\ m^2 s^{-1}, \epsilon = 1.02 \cdot 10^{-4}\ s^{-1}, \alpha = 1 \cdot 10^{-3}\ s^{-1}$). Shaded area represents standard deviation of six simulations.

Discussion

In biomedical applications, like tissue engineering (9) or tumor vascular normalization (10), angiogenesis is stimulated, redirected or reduced to properly vascularize the tissue of interest. Computational models can help understand how different environmental factors and cellular cues affect various aspects of EC migration and network formation and help identify effective regulatory targets. Many computational models of angiogenesis, based on assumptions like cell-cell attraction, cell shape effects, and cell-ECM interaction, have been successful at creating EC networks that resemble those observed *in vitro* qualitatively (18–20). To test whether the manner in which these simulated ECs form networks is also indicative of *in vitro* EC behavior, we selected three cell-based models of 2D angiogenesis based on different assumptions, to examine their dynamical behavior. To quantify dynamical features of *in vitro* EC network formation (Fig 1B) and of simulated EC network formation outcomes of cellular Potts models of 2D angiogenesis we developed a custom image analysis pipeline (Fig 2A) (13,27,28).

We used the outcome of our initial analysis of the *in vitro* and simulated networks to find a parameter space in which the network features of the model outcomes were similar to those of the *in vitro* EC networks (Fig 2C). Within this parameter regime, we conducted further comparisons between the models and the *in vitro* networks to assess if systematic, concurrent parameter changes *in vitro* and *in silico* could help assess the correctness of the models. Interestingly, both chemotaxis-based models showed similar dynamic behavior as the *in vitro* networks. They show an initial cell-cell contact forming phase, followed by a remodeling phase, similar to stages 3 to 5 of *in vitro* network formation: elongation and formation of cell-cell contacts, plexus stabilization, and plexus reorganization. In the mechanical model, however, the ECs quickly form connections, mimicking early *in vitro* network formation, but there is little network reorganization in the model outcomes.

We found that the dynamic behavior of the lacunae in the elongated cell model is most similar to those of the *in vitro* networks (Figs 2D and E). In the elongated cell model the ECs actively elongate before they migrate upwards a chemoattractant gradient (13). Because of their shape, the elongated ECs can form long-range connection to other ECs, and thus form branches and close lacunae more rapidly than

rounded ECs. This improves the similarity of the model to early stages of *in vitro* network formation (Figs 2E and F). Due to the slower movement along the short axis for elongated cells, branches are not very mobile and merge slowly as the network stabilizes (Fig 2F). In the contact inhibition model, the ECs are rounded and less sensitive to the chemoattractant when in contact with other ECs (28). The contact inhibited ECs form a network slower than the elongated ECs (Fig 2E) and this network remodels less (Fig 2F). The contact inhibition model is less robust in reproducing the early stages of *in vitro* angiogenesis, as the initial number of branches is much dependent on the diffusion length (Figs 4D-F). This might be due to an overall lower sensitivity to the chemoattractant due to the contact inhibition. When conducting our search for the optimal diffusion length for the parameter regime in which we compare the networks, we also observed differences in response to changes in decay and secretion rate between the two chemotaxis models. We observe that the contact inhibited ECs require a stronger chemoattractant signal to form a network than the elongated cells. The cell elongation also allows for network formation at lower cell density than the contact inhibition (Figs 4 and S4). From this we can conclude that elongation can help ECs to form networks under circumstances where contact inhibition cannot. The elongated shape of ECs allows for the ECs to sense a chemoattractant gradient at a larger distance from their center of mass, whereas due to contact inhibition ECs become less sensitive to the chemoattractant overall.

It is important to note that the chemoattractant in the simulations can represent any sort of mid-range cell communication signal. Rüdiger *et al.* (2020) argue that mechanical forces are the main driver behind *in vitro* endothelial network formation (4). In this study they continuously perfused the ECs during *in vitro* network formation to wash away any possible chemoattractant gradient, and still observe network formation. To further argue for mechanical regulation, they show that ECs compress the substrate up to a distance of 30 µm, with measurable ECM displacement up to 100 µm. These distances fall within the range of what we observed in the two chemotaxis models similar to the *in vitro* networks. In the mechanical model we observed strains up to 40 µm from the cell boundary in the investigated parameter regime (S2 Fig). However, this was not enough to form networks similar to those observed *in vitro*. In the mechanical model, as it is implemented here, the strain field resets

every MCS and is recalculated based on the current cell shape. *In vitro*, we and others (4,45) observed that ECs remodel the substrate over time, altering its material properties and response to stress. Resetting the strain field each timestep omits any changes in the composition of the environment from the model. This could explain why the EC network in the mechanical model stabilizes quickly, whereas *in vitro* and in the two chemotaxis-based models the EC networks continuously evolve as the simulated chemoattractant gradient gradually stabilizes over time. The effect of matrix remodeling, in the form of strain-stiffening, on EC network formation dynamics could be investigated *in vitro* with synthetic gels with tunable stiffness. With these gels the travel distance of mechanical perturbations on the system can be altered systematically, to measure its effect on EC network formation. With the use of synthetic gels, it is also possible to wash away any chemoattractant from the system, without the possible interference of ECM retention, which might have influenced the network formation in Rüdiger *et al.* (2020).

In the two chemotaxis-based models we assumed each MCS represents 30 seconds in real time and each pixel is 2 µm. This was chosen such that the mean velocity of the cells became 5 $\mu m\ h^{-1}$, which, it was previously argued, complies with *in vivo* observations (13,38). This allows us to translate the physical processes like chemoattractant diffusion and decay rate to physical units ($m^2 s^{-1}$; s^{-1}). We fixed the diffusion coefficient at $D = 5 \cdot 10^{-13}\ m^2 s^{-1}$. The main driver behind angiogenesis is generally assumed to be VEGF-A (39). The diffusion coefficient of VEGF-A is in the order of $10^{-11}\ m^2 s^{-1}$ in collagen-I, $10^{-10}\ m^2 s^{-1}$ in Matrigel and $10^{-9}\ m^2 s^{-1}$ in water (40–42), which is 100 to 10000-fold higher than what we implemented in the model. However, ECM and EC membrane receptor retention of VEGF-A could affect VEGF-A diffusion, resulting in a smaller effective diffusion coefficient and decay rate (6). Köhn-Luque *et al.*, 2013 show an aggregation of fluorescently labeled VEGF in the substrate surrounding HUVECs on Matrigel within 5-10 minutes after VEGF addition (6). Additionally, it is yet unclear whether VEGF-A diffusion is the main driver behind angiogenic network formation *in vitro*. Especially since Rüdiger *et al.* (2020) observed endothelial network formation under constant perfusion to avoid the emergence of a chemical gradient (4). With a diffusion coefficient of $D = 5 \cdot 10^{-13}\ m^2 s^{-1}$ we observe simulated networks most like *in vitro* at a

diffusion length of $l_D = 70\ \mu m$ (Fig 2C). With a diffusion coefficient of $D = 10^{-10}\ m^2 s^{-1}$, the decay rate would need to be $\epsilon = 2 \cdot 10^{-2}\ s^{-1}$ for a diffusion length of $l_D = 70\ \mu m$, since $l_D = \sqrt{\frac{D}{\epsilon}}$, which is much faster than the 90 minute half-life of VEGF-A measured *in vitro* (43). *In vivo*, VEGF-A has been shown to have a half-life of 33.7 minutes (44).

There are some steps in this image analysis pipeline that require optimalization. For example, we implemented a watershed step in the pipeline to correct for breaks in EC branches where thin stretched-out ECs are misinterpreted as background during segmentation. This watershed step can result in an overrepresentation of connections between branches, but overall, we observe an accurate and consistent result (S1 Fig). To circumvent the need for segmentation corrections and other suboptimal parameter settings a neural network could be trained to perform the segmentation steps necessary for the network quantification (37). This network can be trained to recognize thin stretches of ECs where conventional image analysis methods, which rely mostly on contrast, might mistake them for background. However, the training of a neural network requires a lot of correctly annotated training data and undertrained networks will give suboptimal results. More interestingly, a neural network could be trained to recognize network features that are more difficult to extract from segmented images automatically, like cell division events.

Conventional tube formation assays to assess the sprouting ability of ECs are usually only examined for a single characteristic (e.g. number of branches) at a single timepoint (32). However, we observed that network features converged over time independent of their initial observed value (Fig 3B). This indicates that an endpoint observation might not suffice to examine the influence of a compound or knockout on collected cell behavior before a stable network has been formed. We also observed a high biological variation between different samples of the same experimental conditions. This can be explained by variations in fitness of different passage number of ECs and small fluctuations in cell seeding density. Therefore, it is important that the exact number of seeded ECs is also considered when comparing samples within 6 hours after seeding or at low cell densities. Passage number has previously been observed to affect tube formation in mouse 3B-11 endothelial ECs (12). Another

effect on the fitness of the cells could be the duration for which ECs spent outside of the incubator prior to the experiment.

In this work we have shown the importance of dynamic analyses of EC network formation by showing how EC network features converge over time. We paved the way for a more systematic comparison of computational models to biological experiments, and we have indicated areas of improvement for existing cellular Potts models of 2D angiogenesis. In the future we will expand our analysis of EC networks and find new parameter regimes to explore both *in vitro* and *in silico*.

Methods

Cell culture

Immortalized human microvascular endothelial cells (HMEC-1; hereafter ECs) were maintained in T75 flasks (Sarstedt Inc) in MCDB-131 medium (Gibco) supplemented with 10 % fetal calf serum (FCS), 10 ng/mL epidermal growth factor (EGF) (Sigma-Aldrich), 1 µg/mL hydrocortisone (HC) (Thermo Scientific Chemicals), 1 % GlutaMAX (Gibco) and 1 % penicillin/ streptomycin (Gibco). Cells were cultured in a humidified incubator at 37 ˚C and 5 % CO_2 and split twice per week. Passages used were between 9 and 17.

Tube formation assay

Cells at 70-80% confluency were plated on growth factor reduced (GFR) Matrigel (Corning) on Angiogenesis µ-slides (Ibidi) at a density of 10,000 cells per well unless stated otherwise. For fluorescent plasma membrane labeling cells were incubated with PKH67, PKH26 or CellVue Claret (Sigma-Aldrich) in Diluent C as described in (14).

Imaging

All images were captured at a magnification of 10X using a Nikon Ti inverted phase contrast microscope equipped with a DS-Ri2 camera or a Zeiss Axio Observer inverted phase contrast microscope equipped with an AxioCam 705 mono camera with a motorized stage for 24 hours with 15-minute intervals. Fluorescent images were acquired using the Zeiss Colibri multicolor LED light

source. Full well images were created by stitching multiple fields together with the NIS-elements and ZEN Blue software.

Network characterization

Time-lapse images of the full wells were processed and quantified using a custom Fiji/ImageJ pipeline (v1.53f) (Fig. S1). For the segmentation of cells from background the following steps were performed for each slice in the timelapse images: [1] High-frequency features were amplified by first convoluting the phase-contrast image with a Gaussian filter with sigma value of 10 µm, then subtracting the resulting low-frequency image from the original image and finally adding the resulting high-frequency image back to the original image. [2] Hereafter, the local variance in the sharpened images was computed with a radius of 8.75 µm. The local variances were convoluted with a Gaussian filter with a sigma value of 3.5 µm. [3] From the resulting image a threshold was computed with automatic Huang thresholding to create a segmented mask of the network. [4] The mask was then corrected for broken branches by producing a distance map of the lacunae larger than 2000 µm² and watershed segmenting the distance map with a threshold set to 50. Hereafter the smaller lacunae were added back to the watershed network for the final mask.

The branches and nodes within the binary masks were analyzed with the Skeletonize 2D/3D and Analyze Skeleton (2D/3D) plugins applied on a 10x scaled down image to avoid a very noisy skeleton. The lacunae were analyzed with the Analyze Particles plugin. The resulting output includes the number, size, position and shape of the lacunae, and the number, length, position and connectivity of the branches.

All results were exported to CSV files for further analysis in RStudio. This analysis pipeline was automated to process large quantities of time-lapse images sequentially without user input to maximize reproducibility and minimize personal bias in the data analysis. For the validation of the pipeline, we had six independent participants encircle three lacunae and compared the average lacuna area of their selections to automatically segmented images. The automatic segmentation underestimated the lacunae as selected by the participants by 4.2 ± 11.7 % of the average area (n =

15). The difference between two different participants encircling the same lacunae was 4.5 ± 2 % of average area (n = 3) (S1 Fig).

Computational model

The three computational models of angiogenesis (13,27,28) are all based on hybrid cellular Potts models (CPMs). Hybrid CPMs couple a dynamical description of cell behavior based on the CPM with a detail model of the cellular micro-environment, specifically the concentration of extracellular signaling molecules or strains and stresses in the ECM. The cellular Potts model is a cell-based model that focusses on modeling cell-cell interactions and predicting collective cell behavior (36). Cells are represented as collections of lattice sites $\vec{x}$ with an identical index σ_x on a grid, where each index labels a single cell. Each lattice site represents an area of 2 μm x 2 μm in the chemotaxis models and 5 x 5 μm in the mechanical model. To mimic the circular *in vitro* dishes, we labeled all lattice sites outside of a circle with a diameter of 3800 μm sites as boundary sites $\sigma_x = -1$ in the elongated cell and contact inhibition models and as a fixed node in the mechanical model.

Apart from the shapes of the simulation domains, models were used as described previously (13,27,28). Briefly, during a Monte Carlo step (MCS), a time-step in the simulation representing 30 seconds, cells change their shape and move through the lattice by attempting to copy its index to a neighboring lattice site. There are *N* copy attempts per MCS, with *N* the number of lattice sites. If the copy attempt results in a lower effective energy of the system, the copy attempt is accepted. With an effective energy H,

$$H = \sum_{\vec{x},\vec{x}'} J_{\sigma_{\vec{x}},\sigma_{\vec{x}'}} \left(1 - \delta_{\sigma_{\vec{x}},\sigma_{\vec{x}'}}\right) + \lambda_A \sum_{\sigma}(a_\sigma - A_\sigma)^2 + \lambda_L \sum_{\sigma}(l_\sigma - L_\sigma)^2,$$

where $J_{\sigma_{\vec{x}},\sigma_{\vec{x}'}}$ represents the bond energy between a lattice site $\vec{x}$ and its eight second-order neighbors $\vec{x}'$, and λ_A and λ_L represent energy penalties for deviation from a designated target area (A_σ) or target length (L_σ), which we set at 50 and 5 respectively. If the copy attempt does not result in a lower effective energy, the copy is accepted with Boltzmann probability:

$$P(\Delta H) = e^{-\Delta H/T}$$

where T is the "cellular temperature" of the system, a measure of cell motility, which we set at 50, and ΔH the change in the effective energy function.

In the elongated cell and contact inhibition models (13,28) cells secrete a chemoattractant c, which diffuses and degrades in the ECM,

$$\frac{\partial c(\vec{x},t)}{\partial t} = \alpha(1 - \delta_{\sigma_{\vec{x}},0}) - \varepsilon\delta_{\sigma_{\vec{x}},0}c(\vec{x},t) + D\nabla^2 c(\vec{x},t),$$

where $\delta_{\sigma_{\vec{x}},0} = 1$ outside the cells, α is the secretion rate and ε the degradation rate of the chemoattractant and D the diffusion constant of the chemoattractant. An additional term is added to the energy function, which promotes copies upwards the chemoattractant gradient:

$$\Delta H_{chemotaxis} = -\mu(c(\vec{x}') - c(\vec{x})),$$

Where μ is the strength of the chemotactic response, which we set at 1000. For details see (13,28).

In the mechanical cell-cell communication model (27), cells were able to deform the ECM through cell-shape dependent traction forces. The deformations of the ECM are calculated using the finite element method. An additional term is added to the energy function, such that cells respond to the ECM stiffness:

$$\Delta H_{durotaxis} = -g(\vec{x},\vec{x}')\lambda_{durotaxis}(h\big(E(\epsilon_1)\big)(\vec{v}_1 \cdot \vec{v}_m)^2 + h\big(E(\epsilon_2)\big)(\vec{v}_2 \cdot \vec{v}_m)^2,$$

where $g(\vec{x},\vec{x}') = 1$ for cell extensions and $g(\vec{x},\vec{x}') = -1$ for cell retractions, $\lambda_{durotaxis}$ is a parameter which we set at 24, $h(E)$ mimics the influence of the ECM stiffness E as a function of ϵ_1 and ϵ_2, the principal strains, on the tension in the cell-ECM connection, $\vec{v}_m$ gives the copy direction, and v_1 and v_2 are the strain orientations.

The preference for higher stiffness E is implemented as a sigmoid function:

$$h(E) = \frac{\alpha}{1 + \exp\big(-\beta(E - E_{tr})\big)},$$

where α sets the strength of the durotactic response, E_{tr} determines the stiffness where half this strength is reached and β represents the stiffness sensitivity which determines the steepness of the curve. For details see (27).

Statistical analysis

P-values between groups were calculated using an ANOVA test followed by a student t-test. Dataset significance was defined as $p \leq 0.05$ (*); $p < 0.01$ (**); $p < 0.001$ (***); $p > 0.05$ (ns).

Acknowledgments

This publication is part of the 'Mathematics-based strategies for repairing tumour blood vessels' project with project number 865.17.004 of the Vici research program which is financed by the Dutch Research Council (https://www.nwo.nl/). The funders had no role in study design, data collection and analysis, decision to publish, or preparation of the manuscript. This work was performed using the compute resources from the Academic Leiden Interdisciplinary Cluster Environment (ALICE) provided by Leiden University.

References

1. De Palma M, Biziato D, Petrova TV. Microenvironmental regulation of tumour angiogenesis. Nat Rev Cancer. 2017 Aug;17(8):457–74.

2. Potente M, Gerhardt H, Carmeliet P. Basic and Therapeutic Aspects of Angiogenesis. Cell. 2011 Sep 16;146(6):873–87.

3. Jiang X, Wang J, Deng X, Xiong F, Zhang S, Gong Z, et al. The role of microenvironment in tumor angiogenesis. J Exp Clin Cancer Res. 2020 Sep 30;39(1):204.

4. Rüdiger D, Kick K, Goychuk A, Vollmar AM, Frey E, Zahler S. Cell-Based Strain Remodeling of a Nonfibrous Matrix as an Organizing Principle for Vasculogenesis. Cell Rep. 2020 Aug 11;32(6):108015.

5. Reinhart-King CA, Dembo M, Hammer DA. Endothelial Cell Traction Forces on RGD-Derivatized Polyacrylamide Substrata. Langmuir. 2003 Mar 1;19(5):1573–9.

6. Köhn-Luque A, Back W de, Yamaguchi Y, Yoshimura K, Herrero MA, Miura T. Dynamics of VEGF matrix-retention in vascular network patterning. Phys Biol. 2013 Dec;10(6):066007.

7. Hellström M, Phng LK, Hofmann JJ, Wallgard E, Coultas L, Lindblom P, et al. Dll4 signalling through Notch1 regulates formation of tip cells during angiogenesis. Nature. 2007 Feb;445(7129):776–80.

8. Lampugnani MG, Zanetti A, Corada M, Takahashi T, Balconi G, Breviario F, et al. Contact inhibition of VEGF-induced proliferation requires vascular endothelial cadherin, β-catenin, and the phosphatase DEP-1/CD148. J Cell Biol. 2003 May 26;161(4):793–804.

9. Mastrullo V, Cathery W, Velliou E, Madeddu P, Campagnolo P. Angiogenesis in Tissue Engineering: As Nature Intended? Front Bioeng Biotechnol. 2020;8:188.

10. Jain RK. Antiangiogenesis strategies revisited: from starving tumors to alleviating hypoxia. Cancer Cell. 2014 Nov 10;26(5):605–22.

11. Nowak-Sliwinska P, Alitalo K, Allen E, Anisimov A, Aplin AC, Auerbach R, et al. Consensus guidelines for the use and interpretation of angiogenesis assays. Angiogenesis. 2018 Aug;21(3):425–532.

12. DeCicco-Skinner KL, Henry GH, Cataisson C, Tabib T, Gwilliam JC, Watson NJ, et al. Endothelial Cell Tube Formation Assay for the In Vitro Study of Angiogenesis. J Vis Exp JoVE. 2014 Sep 1;(91):51312.

13. Merks RMH, Brodsky SV, Goligorksy MS, Newman SA, Glazier JA. Cell elongation is key to in silico replication of in vitro vasculogenesis and subsequent remodeling. Dev Biol. 2006 Jan 1;289(1):44–54.

14. Parsa H, Upadhyay R, Sia SK. Uncovering the behaviors of individual cells within a multicellular microvascular community. Proc Natl Acad Sci U S A. 2011 Mar 22;108(12):5133–8.

15. Reinhart-King CA, Dembo M, Hammer DA. The Dynamics and Mechanics of Endothelial Cell Spreading. Biophys J. 2005 Jul 1;89(1):676–89.

16. Califano JP, Reinhart-King CA. Substrate Stiffness and Cell Area Predict Cellular Traction Stresses in Single Cells and Cells in Contact. Cell Mol Bioeng. 2010 Mar 1;3(1):68–75.

17. Sharpe J. Computer modeling in developmental biology: growing today, essential tomorrow. Development. 2017 Dec 1;144(23):4214–25.

18. Zhang Y, Wang H, Oliveira RHM, Zhao C, Popel AS. Systems biology of angiogenesis signaling: Computational models and omics. WIREs Mech Dis. 2022;14(4):e1550.

19. Subramanian A, Zakeri P, Mousa M, Alnaqbi H, Alshamsi FY, Bettoni L, et al. Angiogenesis goes computational – The future way forward to discover new angiogenic targets? Comput Struct Biotechnol J. 2022 Jan 1;20:5235–55.

20. Miura T. Theoretical Models of Vascular Pattern Formation. Fukuoka Igaku Zasshi Hukuoka Acta Medica. 2016 Sep;107(9):161–8.

21. Manoussaki D, Lubkin SR, Vernon RB, Murray JD. A mechanical model for the formation of vascular networks in vitro. Acta Biotheor. 1996 Nov;44(3–4):271–82.

22. Serini G, Ambrosi D, Giraudo E, Gamba A, Preziosi L, Bussolino F. Modeling the early stages of vascular network assembly. EMBO J. 2003 Apr 15;22(8):1771–9.

23. Palachanis D, Szabó A, Merks RMH. Particle-based simulation of ellipse-shaped particle aggregation as a model for vascular network formation. Comput Part Mech. 2015 Dec 1;2(4):371–9.

24. Metzcar J, Wang Y, Heiland R, Macklin P. A Review of Cell-Based Computational Modeling in Cancer Biology. JCO Clin Cancer Inform. 2019 Feb;3:1–13.

25. Merks RMH, Glazier JA. A cell-centered approach to developmental biology. Phys Stat Mech Its Appl. 2005 Jul 1;352(1):113–30.

26. Vega R, Carretero M, Travasso RDM, Bonilla LL. Notch signaling and taxis mechanisms regulate early stage angiogenesis: A mathematical and computational model. PLOS Comput Biol. 2020 Jan 27;16(1):e1006919.

27. van Oers RFM, Rens EG, LaValley DJ, Reinhart-King CA, Merks RMH. Mechanical Cell-Matrix Feedback Explains Pairwise and Collective Endothelial Cell Behavior In Vitro. PLOS Comput Biol. 2014 Aug;10(8):1–14.

28. Merks RMH, Perryn ED, Shirinifard A, Glazier JA. Contact-Inhibited Chemotaxis in De Novo and Sprouting Blood-Vessel Growth. PLOS Comput Biol. 2008 Sep 19;4(9):e1000163.

29. Dejana E. Endothelial cell–cell junctions: happy together. Nat Rev Mol Cell Biol. 2004 Apr;5(4):261–70.

30. Gory-Fauré S, Prandini MH, Pointu H, Roullot V, Pignot-Paintrand I, Vernet M, et al. Role of vascular endothelial-cadherin in vascular morphogenesis. Development. 1999 May 15;126(10):2093–102.

31. Stéphanou A, Meskaoui G, Vailhé B, Tracqui P. The rigidity in fibrin gels as a contributing factor to the dynamics of *in vitro* vascular cord formation. Microvasc Res. 2007 May 1;73(3):182–90.

32. Carpentier G, Berndt S, Ferratge S, Rasband W, Cuendet M, Uzan G, et al. Angiogenesis Analyzer for ImageJ — A comparative morphometric analysis of "Endothelial Tube Formation Assay" and "Fibrin Bead Assay." Sci Rep. 2020 Jul 14;10(1):11568.

33. Sartorius [Internet]. [cited 2023 May 6]. Live Cell Analysis Instruments. Available from: https://www.sartorius.com/en/products/live-cell-imaging-analysis/live-cell-analysis-instruments

34. Tube Formation Image Analysis | WimTube | Wimasis [Internet]. [cited 2023 May 6]. Available from: https://www.wimasis.com/en/WimTube

35. ibidi [Internet]. [cited 2023 May 6]. Tube Formation FastTrack AI Image Analysis Software. Available from: https://ibidi.com/software-and-image-analysis/189-tube-formation-fasttrack-ai-image-analysis.html

36. Glazier JA, Graner F. Simulation of the differential adhesion driven rearrangement of biological cells. Phys Rev E. 1993 Mar 1;47(3):2128–54.

37. Davidson CD, Wang WY, Zaimi I, Jayco DKP, Baker BM. Cell force-mediated matrix reorganization underlies multicellular network assembly. Sci Rep. 2019 Jan 9;9:12.

38. Rupp PA, Czirók A, Little CD. αvβ3 integrin-dependent endothelial cell dynamics in vivo. Development. 2004 Jun 15;131(12):2887–97.

39. Carmeliet P. VEGF as a Key Mediator of Angiogenesis in Cancer. Oncology. 2005;69(3):4–10.

40. Jeong GS, Han S, Shin Y, Kwon GH, Kamm RD, Lee SH, et al. Sprouting Angiogenesis under a Chemical Gradient Regulated by Interactions with an Endothelial Monolayer in a Microfluidic Platform. Anal Chem. 2011 Nov 15;83(22):8454–9.

41. Miura T, Tanaka R. *In vitro* Vasculogenesis Models Revisited - Measurement of VEGF Diffusion in Matrigel. Math Model Nat Phenom. 2009;4(4):118–30.

42. Shin Y, Han S, Jeon JS, Yamamoto K, Zervantonakis IK, Sudo R, et al. Microfluidic assay for simultaneous culture of multiple cell types on surfaces or within hydrogels. Nat Protoc. 2012 Jul;7(7):1247–59.

43. Kleinheinz J, Jung S, Wermker K, Fischer C, Joos U. Release kinetics of VEGF165 from a collagen matrix and structural matrix changes in a circulation model. Head Face Med. 2010 Jul 19;6:17.

44. Eppler SM, Combs DL, Henry TD, Lopez JJ, Ellis SG, Yi JH, et al. A target-mediated model to describe the pharmacokinetics and hemodynamic effects of recombinant human vascular endothelial growth factor in humans. Clin Pharmacol Ther. 2002;72(1):20–32.

45. Maška M, Ulman V, Delgado-Rodriguez P, Gómez-de-Mariscal E, Nečasová T, Guerrero Peña FA, et al. The Cell Tracking Challenge: 10 years of objective benchmarking. Nat Methods. 2023 Jul;20(7):1010–20.

Supporting information

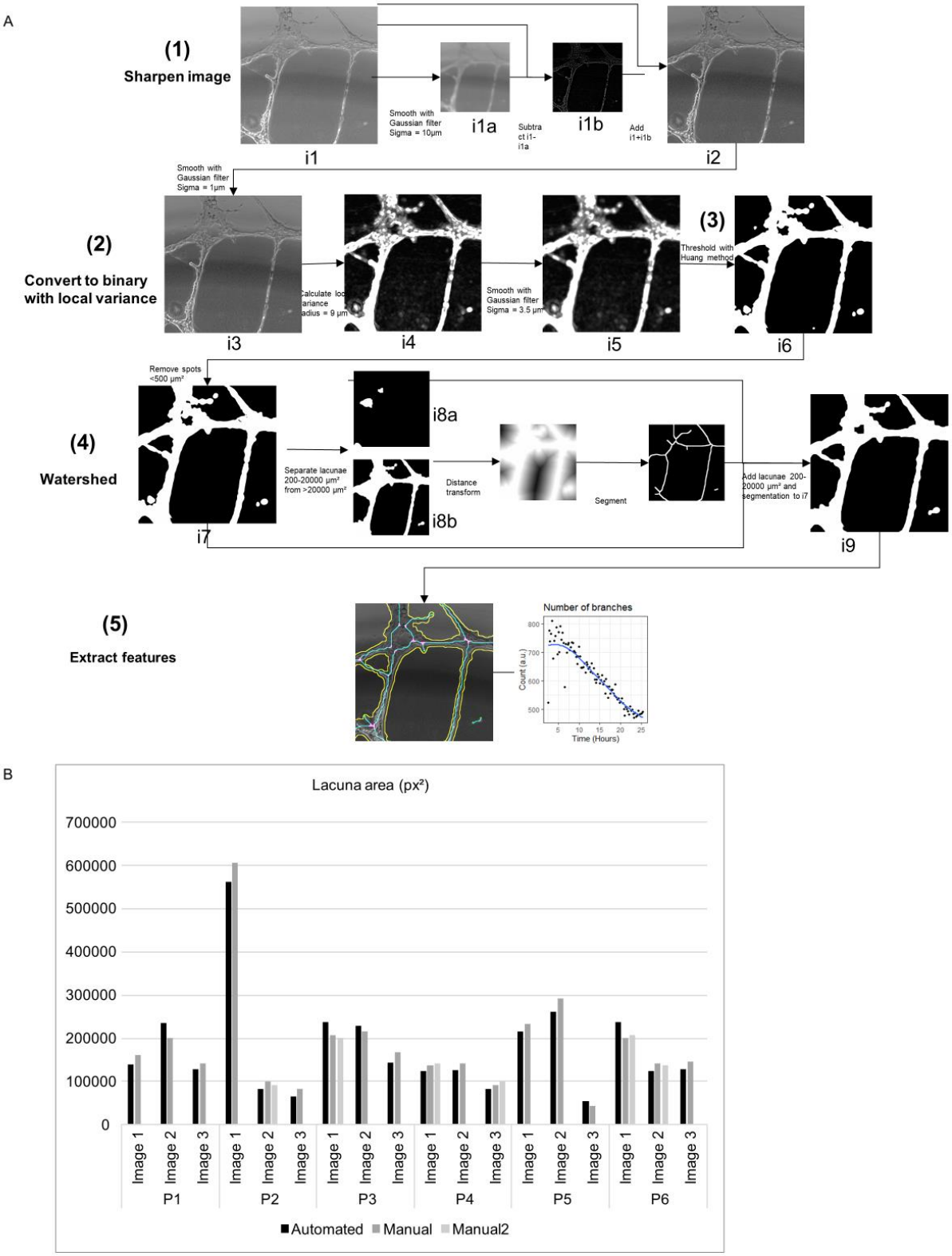

S1 Fig. A) A detailed scheme of the image analysis pipeline showing intermediate images. B) A comparison between lacunae area measured by independent peers and automatically segmented lacunae.

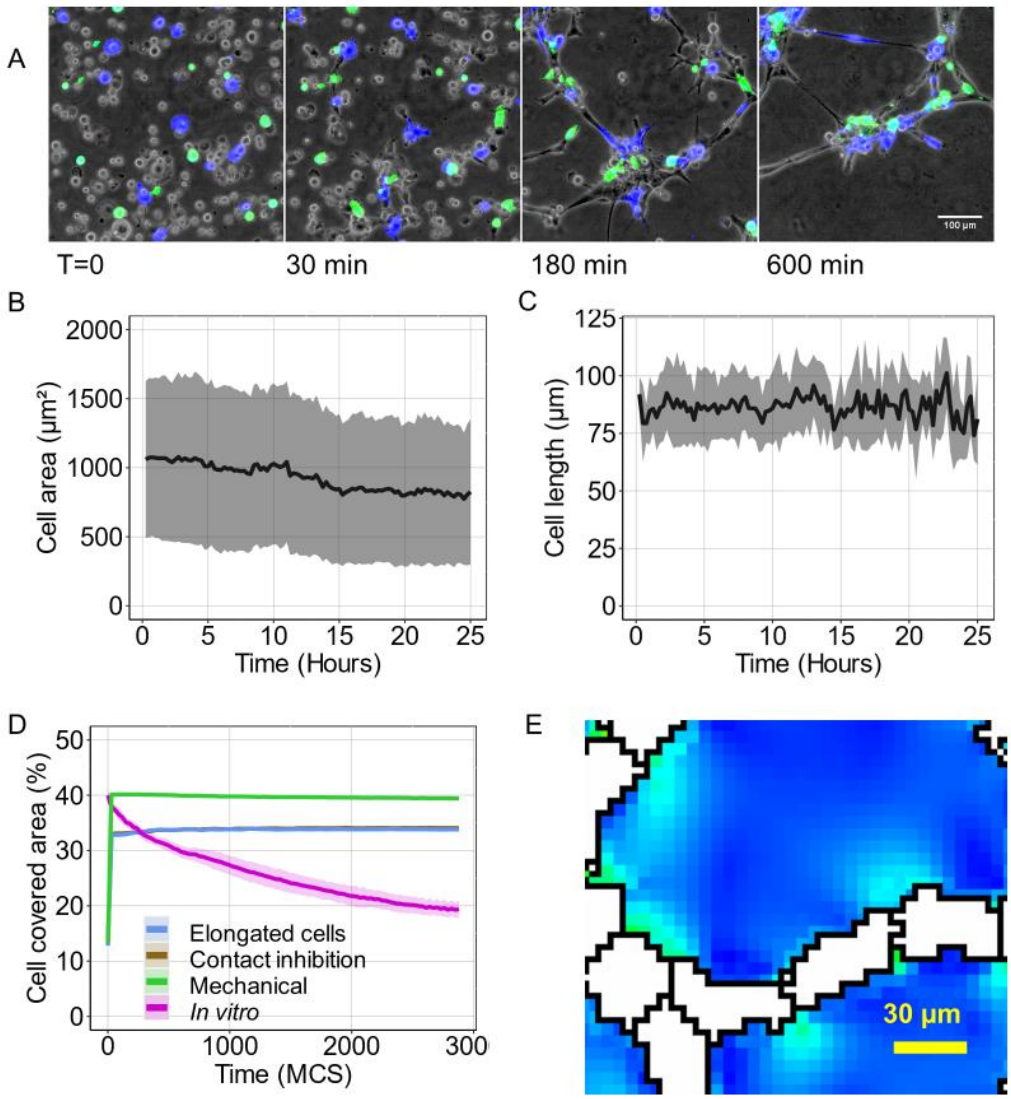

S2 Fig. A) ECs were labeled using membrane linker dyes and segmented from the background. B) The average area of fluorescently labeled ECs over 24 hours. (n > 600 per timestep) C) The average cell length of elongated cells over time (Area between 500 and 1500 µm²; roundness below 0.25) (n > 6 per timestep). D) Cell covered area was measured as a percentage of the total well area. Shaded areas represent the standard deviation. C) ECs (white) in the mechanical model exert strain on their environment indicated by blue green heatmap.

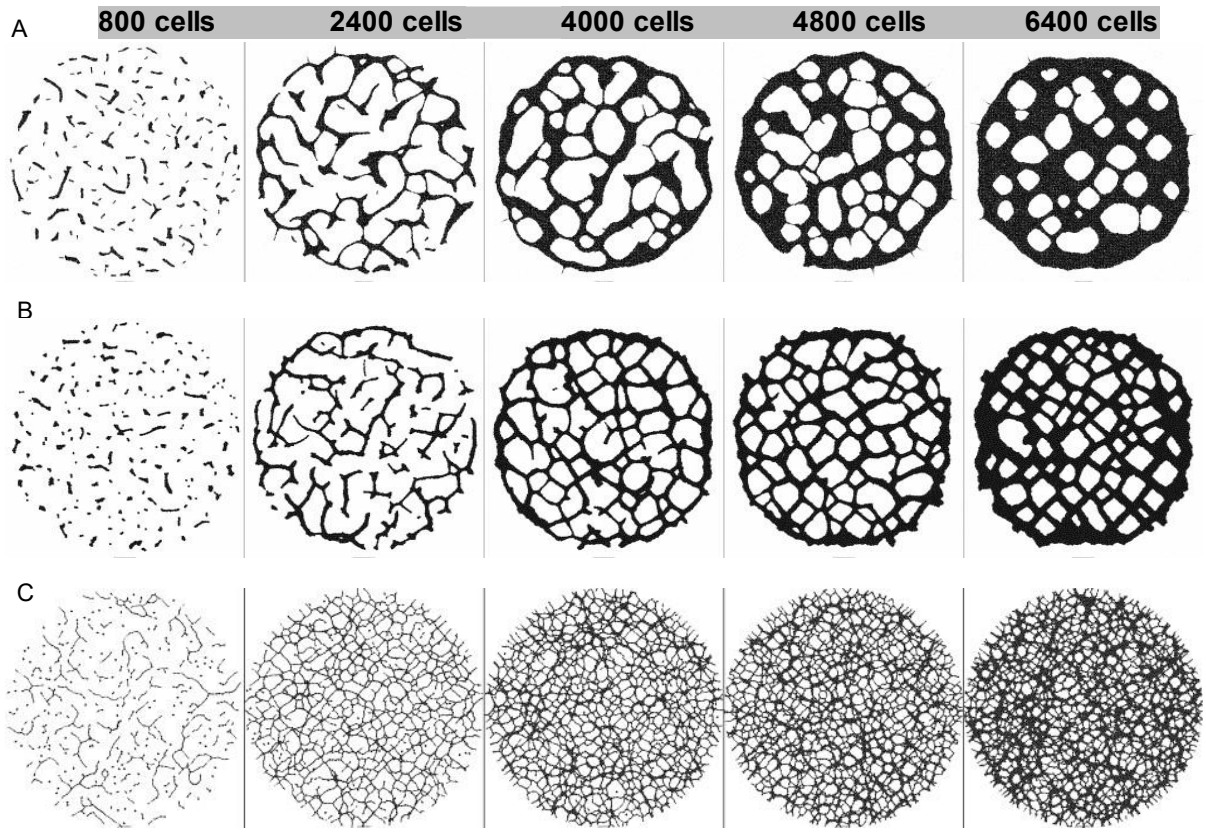

S3 Fig. Overview images of simulated networks for different cell densities after 2880 MCS. A) Elongated cell model. B) Contact inhibition model. C) Mechanical model.

S1 Table. Chemotaxis model parameters

Parameter	**Value**	**Unit**
Pixel size	2e-6	m
Field diameter	1900	pixels
CPM temperature	50	-
Cell target area	250	pixels
Initial cell diameter	12	pixels
Strength of area constraint	50	-
Strength of length constraint	5	-
Connectivity dissipation	5000	$N\ m^{-1}$
Cell-medium contact cost	20	-
Cell-cell contact cost	40	-
Chemotaxis strength	1000	$N\ m^{-1}$
Relaxation time	100	MCS
Border energy	100	$N\ m^{-1}$
Order of neighborhood	2	-
Diffusion coefficient	5e-13	$m^2\ s^{-1}$
Secretion rate	1e-3	s^{-1}
PDE time increment	2	s
PDE iterations per MCS	15	-

S2 Table. Mechanical model parameters

Parameter	**Value**	**Unit**
Pixel size	0.000005	m
Field diameter	760	pixels
CPM temperature	1	-
Cell target area	40	pixels
Strength of area constraint	10000	-
Cell force	1	$N\ m^{-1}$
Cell-medium contact cost	500000	m^{-1}
Cell-cell contact cost	1000000	m^{-1}
Young's modulus	12000	Pa
Poisson's ratio	0.45	-
Accuracy of solver	0.00001	-
Strength of durotaxis	24	-
Threshold for stiffness preference	15000	Pa
Strain stiffening parameter	0.1	-